High Power and Contamination Properties of All-Silica High Reflectivity Multilayers

Phyo Lin, Merlin Mah, Joseph Randi, Sage DeFrances, David Bernot, and Joseph J. Talghader

***Abstract*—Optical multilayers created from a single material have been demonstrated to have lower stress and lower thermal expansion mismatch than standard two-material coatings; however, questions of high power operation and vulnerability to environmental contamination remain. This study examines the particle-induced laser damage properties of all-silica high reflectivity multilayers, specifically those for high average power illumination. All-silica infrared reflectors were deposited by oblique angle deposition (OAD). All-silica mirrors showed low overall stress and had smaller stress changes with temperature. Their laser-induced damage thresholds (LIDTs) under high-power continuous wave (CW) laser illumination with carbon particulate contamination are significantly higher than corresponding high reflectivity multilayers composed of two materials.**

***Index Terms*—High-energy laser optics, laser-induced damage, mirrors, multilayers, particle contamination, optical thin films.**

I. Introduction

OPTICS for high power applications must meet high mechanical and dielectric standards. Large stresses due to heating and thermal expansion mismatch can cause cracking [1], buckling [2], delamination [3], and substrate deformation [4], among other issues. It is well-known that low density films tend to have lower stresses than high density ones [5]; therefore, a complex multilayer containing a significant fraction of low density layers may be more resistant to stress-related failure than high-density coatings with high (usually compressive) stresses.

However, lower density dielectric coatings often display less stability to environmental factors such as humidity or contamination. For example, low density coatings will often have an index of refraction value that can change in an environment with different humidity. Likewise, low density coatings have surface and porosity characteristics that are thought to attract contaminants and particulates more than high density films [6], [7], [8] and this characteristic can sometime propagate through non-conformal higher density coatings placed above them [9], [10]. While the former problem of humidity can be mitigated with relatively simple conformal protective coatings [11], the latter problem would present a strong argument against low density thin films in high average power applications because their particle-based laser breakdown would be greatly impacted. From an alternative perspective, designers making coatings from a single material can choose the absolutely optimal material from the perspective of bandgap, dielectric constant, thermal conductivity, thermal expansion, and many other parameters. In this paper, we examine contamination-induced laser breakdown on single-material low density coatings.

Continuous wave and long-pulse excitation [12] typically leads to direct thermal damage in the form of melting [13], thermal expansion deformation [14], or microcracks [15] and thermal shock damage [16]. Short pulse laser damage is typically based on high field effects such as multiphoton absorption [17], [18] or impact ionization [19], [20], and the laser induced damage threshold (LIDT) shows a strong dependence on the bandgap of the constituent materials. Recently it has been noted that continuous-wave laser damage of particle-contaminated surfaces ironically has a strong bandgap dependence similar to that seen for clean ultra-short pulse damage [21]. Since most failures of high power optics in commercial or military use are random failures at power levels far below laboratory ultra-short pulse LIDT levels, it is suspected that particle contamination is a major culprit. The physical explanation of this effect is that laser radiation is absorbed by a contaminant particle on the surface of the coating. Energy from particle absorption and heat transfer across the particle-film interface raises the temperature of the film surface to extremely high temperatures and excites free carriers in the film. The generated carrier concentration depends on the bandgap of the materials. The generated free carriers then absorb more laser light subsequently, which may cause runaway thermal breakdown. However, if a contaminant particle fully evaporates before breakdown threshold is reached, the process stops, and the optic will survive.

Since the particle-induced CW LIDT increases with increasing bandgap of materials, a material with a high bandgap must be used. Since silicon dioxide films are extremely common and have an extremely high bandgap [22], multilayers films composed of alternating layers of high and low-density silica offer the promise of optimal stress and potentially the highest contamination-induced laser damage threshold. However, low-density films and multilayers often have higher surface

Manuscript received June 17, 2021; revised July 9, 2021; accepted July 26, 2021. Date of publication July 29, 2021; date of current version August 24, 2021. This work was supported in part by the Joint Directed Energy Transition Office and in part by the Office of Naval Research under Grant N00014-17-1-2438. Portions of this work were conducted in the Minnesota Nano Center, which is supported by the National Science Foundation through the National Nano Coordinated Infrastructure Network (NNCI) under Award Number ECCS-2025124. *(Corresponding author: Phyo Lin.)*

Phyo Lin, Merlin Mah, and Joseph J. Talghader are with the Electrical Engineering Department, University of Minnesota, Minneapolis, MN 55455 USA (e-mail: linx0921@umn.edu; merlin@umn.edu; joey@umn.edu).

Joseph Randi, Sage DeFrances, and David Bernot are with the Electro Optics Center, Pennsylvania State University, Freeport, PA 16229 USA (e-mail: jar39@arl.psu.edu; sbd149@arl.psu.edu; dmb40@arl.psu.edu).

Digital Object Identifier 10.1109/JPHOT.2021.3100803

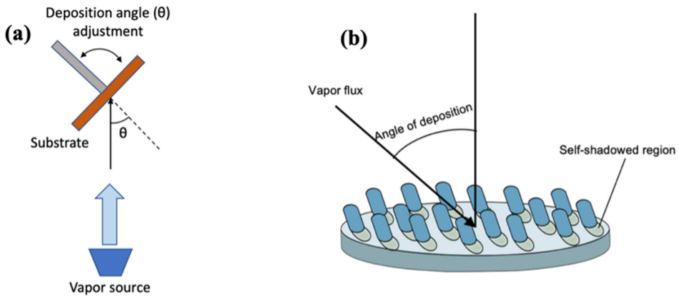

Fig. 1. Conceptual diagrams of (a) oblique angle deposition (OAD), (b) self-shadowing effect.

roughness than high density films, and this may cause unwanted particle-surface interactions[8], [21], and this can propagate even if the low-density film is not the top layer. It must be verified that surface interactions between particles and a low-density coating do not cause unusual behavior with respect to laser damage.

Although prior studies have been done on the optical properties (usually in UV range) of all-silica multilayers [23], [24], their contamination-induced laser breakdown remains uninvestigated. We examined high reflectivity (HR) multilayers composed of alternating layers of low- and high-density silica. SiO_2 nanocolumnar films, deposited by oblique angle deposition (OAD) techniques, showed very low stresses at high deposition angles. Bilayer all-silica samples showed higher contamination-induced laser damage thresholds than other common optical materials deposited under similar conditions. Also, the particle-induced LIDT of all-silica HR coatings were compared to that of standard HR mirrors. Carbon-particle-contaminated all-silica coatings survived an irradiance of 3 MW/cm^2, whereas similarly contaminated hafnia/silica, silicon oxynitride/silica, and tantala/silica HR coatings failed catastrophically. Moreover, the stresses of all-silica stacks were lower than other ALD-deposited oxides and offer advantages in thermal expansion due to having only a single material. These advantageous properties make all-silica coatings a significant candidate for future high power laser applications.

II. Sample Fabrication

Three types of samples were deposited as part of the film development of this study: single layer, bilayer, and multilayer high reflectivity (HR). All of the low density films were SiO_2 films deposited by oblique angle deposition (OAD) [25] in an electron beam evaporator (Varian model: 3118) with a high-voltage electron gun at 4 kV and an emission current ranging from 3 to 6 mA. The e-beam evaporator was backfilled with an oxygen partial pressure of $9x10^{-5}$ Torr. As shown in Fig. 1(a), the substrate is held directly above the vapor source on a sample holder with angle adjustment capability so that the film is deposited at an oblique angle with respect to the direction of vapor flux. This introduces a self-shadowing effect [26], which prevents regions behind the initial nuclei from receiving vapor and allows collimated nanorods to form as shown in Fig. 1(b). The initial individual silica films of this study were deposited

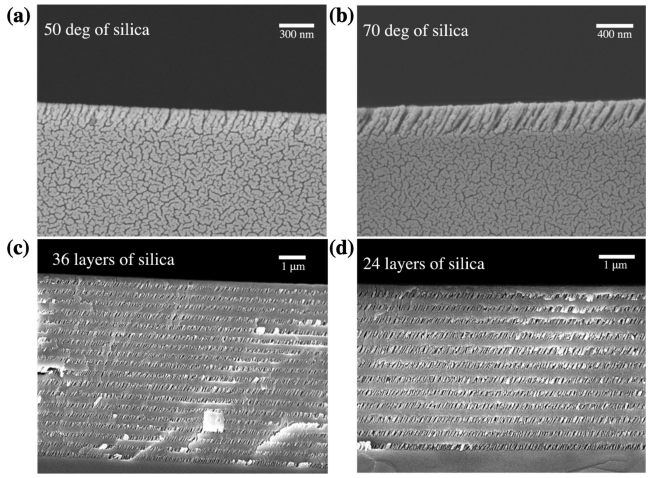

Fig. 2. SEM pictures of (a) 50-degree porous silica, (b) 70-degree porous silica, (c) 36-layered all-silica HR and (d) 24-layered all-silica HR. All-silica HRs were made of alternating layers of fully dense silica deposited at a 0° angle and porous silica deposited at a 70° angle.

at 50°, 60°, 70° and 75° angles. The density and porosity of the film were controlled by changing the deposition angle. The SEM images of silica films deposited at 50° and 70° angles are shown in Fig. 2(a) and (b), which show higher deposition angle gives more slanted columns and bigger gaps (pores).

All-silica bilayer and HR coating samples were fabricated by using alternate layers of fully dense silica, deposited at a 0-degree angle as a high index layer, and nanocolumnar silica, deposited at a 70-degree angle as a low index layer. HR coatings were designed for a center wavelength of 1070 nm, and the required quarter wave thicknesses were calculated to be 188 nm for the fully dense layer and 214 nm for the nanocolumnar layer. To minimize contamination, multiple layers were deposited during each run without opening the chamber by utilizing the mechanical sample holder with a rotation axis that can be controlled from outside of chamber. A quartz crystal sensor, held near the sample holder, monitored and maintained deposition rates of approximately 6 Å/s for the dense silica layers and 4 Å/s for the nanocolumnar silica layers. Since the thickness measured by the crystal sensor does not directly represent the thickness of our films because of the change in density between them, calibration measurements need to be made at each density to obtain an accurate mapping between crystal monitor signal and film thickness. The crystal monitor needed to be replaced with a new one several times throughout the processes of this paper to maintain a good thickness control. Scanning electron microscope (SEM) pictures of two all-silica mirrors are shown in Fig. 2(c) and (d).

Several bilayer and HR samples using non-silica materials were also deposited to provide a comparison to the all-silica samples. The bilayers consisted of a bottom layer of alumina, hafnia, titania, or aluminum nitride deposited using atomic layer deposition (ALD), with a top layer of evaporated high density silica. High density silica was chosen as the top layer for all bilayers since a high density cap layer has been previously found useful in enhancing the environmental stability of coatings in

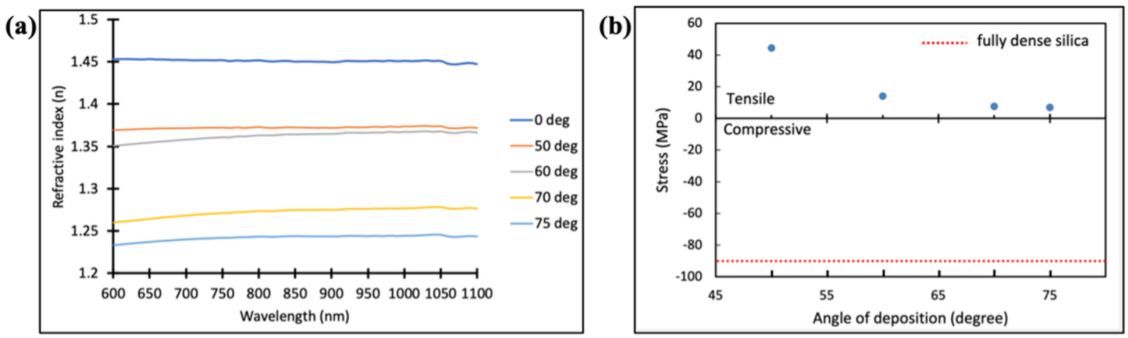

Fig. 3. (a) Refractive indices of low density silica deposited at different vapor incident angles. The refractive index decreases with increasing porosity at high deposition angles. (b) The stresses of individual porous silica layers at different deposition angles. Tensile stress decreases as pore size increases at very high deposition angles.

general [11]. The HR samples were deposited on fused silica substrates of two different thicknesses, 0.5 mm with 2 inch diameter and 6.3 mm with 1 inch diameter. The thin substrates hosted multiple layers of silicon oxynitride and silica deposited using a plasma-enhanced chemical vapor deposition (PECVD-Plasmatherm 790) system at 250 °C. Oxynitride layers were deposited at a power of 20 W and a pressure of 900 mTorr, with gas flows of 100 sccm SiH_4/HE, 15 sccm N_2O, 15 sccm NH_3 and 98 sccm N_2. Silica layers were deposited at the same power and pressure with gas flows of 200 sccm SiH_4/He and 450 sccm N_2O. The refractive index of the oxynitride was tuned so that the index contrast between the high and low index layers was approximately the same as the all-silica HR coatings. On the thick substrates, the coating company, Advanced Thin Films (ATF), deposited high reflectivity hafnia/silica and tantala/silica distributed Bragg reflector (DBR) mirrors designed for a wavelength of 1070 nm using ion-beam sputtering (IBS).

Carbon microparticles were chosen as contaminants for LIDT testing since generic carbon contamination is often encountered outside of a cleanroom environment. Particles with an average size of 7 um was mixed in isopropyl alcohol to create a solution. Six droplets of carbon-mixed solution were put onto the surface of the sample and spin coated at 1000 rpm for 30s, with a ramp of 200 rpm/s. The solution was dried with compressed nitrogen flow, which left carbon microparticles adhered to the samples. The samples were then characterized using an optical microscope with a home-built particle counting program to make sure the particle spread was consistent across the areas of interest. Particles were found to attach similarly on all samples as they all have high-density silica as a top layer. The contaminated samples were then tested for their contamination-induced damage thresholds.

III. Measurements and Discussion

A. Individual Porous Silica Layer

The refractive indices of the single layer silica films were measured using a spectroscopic ellipsometer [27] over a wavelength range of 600 to 1100 nm. Fig. 3(a) shows the dispersion relationship for silica films deposited at several different angles. Our fully dense silica layers were measured to have a refractive index around 1.46, which is the common value for silica films. As the deposition angle gets higher, the porosity increases, and the refractive index of the film decreases. The lowered index is primarily due to the replacement of silica material in the gaps between silica nano-columns with air and water vapor.

The stress of the films was measured using standard substrate curvature [28]. The substrate's radius of curvature was measured using a Frontier Semiconductor film stress measurement (FSM-900TC) system before and after a film was deposited. The stress was then calculated using Stoney's equation [29] or a more general form of elastic deformation equation [30], [31]. The stresses of individual layers deposited at 0°, 50°, 60°, 70°, and 75° were measured, and the results, as shown in Fig. 3(b), indicated that the stress switches from compressive to tensile as the film gains porosity. However, a relaxation in tensile stress was observed as the deposition angle, and hence pore size, increase. Both mechanisms can be explained by water-adsorption stress induced by vapor trapped inside pores [32].

Although very low index films can be obtained by depositing at very high deposition angles, it was found to be very hard to maintain thickness uniformity of the film at deposition angles higher than 70° with our current evaporator setup. With this finding in mind, our nanocolumnar (or porous) silica was deposited at 70°, with a corresponding refractive index of around 1.27. These conditions were used for the low index layer in all multilayer deposition. The resulting difference in refractive indices between fully dense and porous silica was then 0.19, resulting in a $\Delta n/n_{Silica}$ ratio of about 0.13. This value is lower than the most common HR reflector pairs, such as HfO_2/SiO_2 ($\Delta n/n_{Silica} = 0.3$) and Ta_2O_5/SiO_2 ($\Delta n/n_{Silica} = 0.4$), but it still proved easily sufficient to fabricate our HR mirrors.

B. All-Silica Multilayers

The reflectivities of our all-silica HR mirrors was measured using the set-up shown in Fig. 4. This system has two optical paths: one is a reference that travels around the sample into the detector, and another is the actual signal which follows largely the same path except of course for the reflection off of the sample. The two paths are optically chopped by different frequencies using an optical chopper and combined at a lock-in amplifier to remove background noise, where the sample signal is divided by

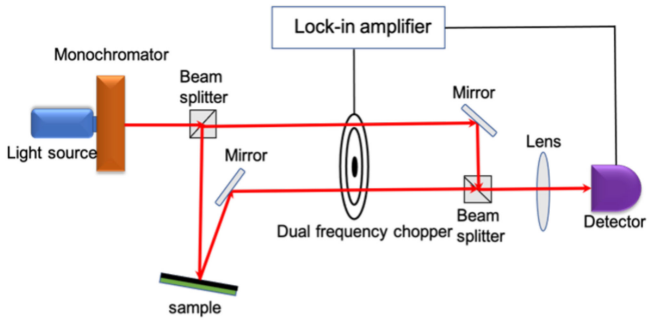

Fig. 4. Experimental set-up diagram for reflectivity measurements.

the reference. Prisms split and recombined the light at the light source and detector, respectively. This set-up corrects for any wavelength-dependent variations at the light source, detector, or other components, so that they do not affect the final reflectivity data. The light path incident onto the sample slightly deviates from 0° so that the reflected beam can be isolated from the incident one. A limitation of this technique is that the absolute numerical reflectivity is not measured but rather a ratio relative to the peak intensity of the optical reference path.

Based on this ratio, the all-silica HR mirrors had a peak reflectivity approximately 80% at 24 layers and 90% at 36 layers as shown in Fig. 5. The reflectivity peak agrees reasonably closely with our calculated value from matrix simulation [33], which are approximately 83% for 24 layers and 93% for 36 layers. However, we note that due to the need to measure stress several times during deposition and, indeed, the lack of real-time control of our evaporation system, the sample reflectivities were measured multiple times between deposition runs and the deposition rates adjusted to obtain a reflectivity peak at the right wavelength, which caused some distortion in the reflectivity profile of the side lobes. The samples have a somewhat narrower reflection bandwidth than standard HRs due to the somewhat smaller index contrast between the high density and low density silica layers. If desired, the reflectivity can be improved by depositing additional layers or developing a more uniform extremely-high-angle deposition process.

A photothermal common-path interferometer (PCI) [34] (Stanford Photo-Thermal Solutions Quad PCI) was used to measure the absorptions of our samples. In this setup, a 10 W 1064 nm high power IPG pump laser was focused onto the surface of the sample. This heats a local area, which is simultaneously probed by a low power He-Ne laser with a larger spot size. The heated area expands and changes refractive index, both of which cause a phase shift between the center and edges of the probe signal. The probe is focused onto a detector, where the intensity tracks the relative phase offset between center and edge. Software then estimates an absorption value in ppm based on this data. The laser beams were scanned over a 0.5 mm × 0.5 mm area of the surfaces of each bilayer and HR sample. Occasional spots with much higher absorption than average are almost always noted in all types of samples (not just all-silica), and these are usually interpreted as unwanted particles or other defects on the sample surface. Disregarding these points, the absorptions of most samples of different optical materials are low and comparable as shown in Fig. 6, except for the titania/silica bilayer sample, which we suspect as being deposited oxygen poor. The absorption of all-silica HR coating is quite good with an absorption of 20 ppm on average, which is higher than that for the all-silica bilayers at around 5 ppm, owing to the smaller number of layers on the latter structure.

Laser damage testing took place at the Penn State ElectroOptics Center using a 12 kW CW Ytterbium-doped IPG Photonics fiber laser (IPG YLS-17000) at 1070 nm. Since we are interested in contamination-induced damage thresholds, all our samples were contaminated with carbon particles on their surfaces before the experiment. This procedure allows large surface areas to be illuminated at power density levels that can cause failure, and the resulting power density levels are more typical of failure of optics in the field than traditional ultra-short pulse experiments where failure occurs at intensities many orders of magnitude higher than would ever be seen in a CW laser system. We note that there may be proximity effects between particles, and, indeed, the measured laser damage threshold depends on the density of contaminants. To minimize this effect, our samples were characterized with an optical microscope and home-built particle counting program, as described previously, to make sure there is a consistent statistical distribution of carbon particles across all samples. A large beam size(1mm) was used in laser damage testing to cover areas with similar particle distributions, averaging over many contaminants, which allows our samples to have a statistically similar coupling between contaminant particles. However, we admit that the complex issue of the impact of particle position and mass distribution on laser damage threshold has not been fully explored. We note that none of our samples would be expected to fail in CW tests at these power levels in the absence of contamination, with the possible exception of titania. (Note that titania has such a small bandgap that one sometimes sees random failures in this material even under nominally clean uncontaminated CW damage conditions.)

The experiments were performed using fused silica substrates of two different thicknesses (as described previously), thin (0.5 mm) and thick (6.3 mm). Each material layer used in all our samples was designed for a quarter-wave at 1070 nm. The total thickness does not matter significantly since laser damage occurs near the surface based on carbon contamination, which increases the absorption mainly based on bandgap of the materials [21]. Bilayer silica samples on thin substrates were tested to observe how resistant all-silica is as an optical coating compared to other ALD deposited bilayer oxides under the same conditions. Three samples (each from the same deposition run) of each type, AlN/SiO_2, TiO_2/SiO_2, HfO_2/SiO_2 and Al_2O_3/SiO_2, were tested. One sample from each type was used in the first testing run at varying irradiance levels to determine where failure occurred. The rest of the samples were then tested at much narrower range of irradiance levels from slightly below damage to slightly above damage. This procedure explains the characteristic and repeated spread in data seen between high and low data points for each material. Fig. 7(a) shows that the all-silica samples had higher LIDT than the other materials, and most materials showed a strong bandgap dependence. The one material type that did

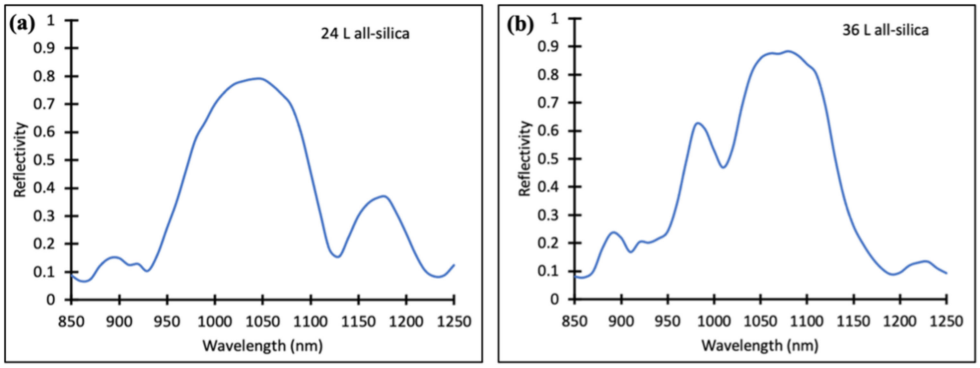

Fig. 5. Reflectivities of (a) 24-layered all-silica coating and (b) 36-layered all-silica coating.

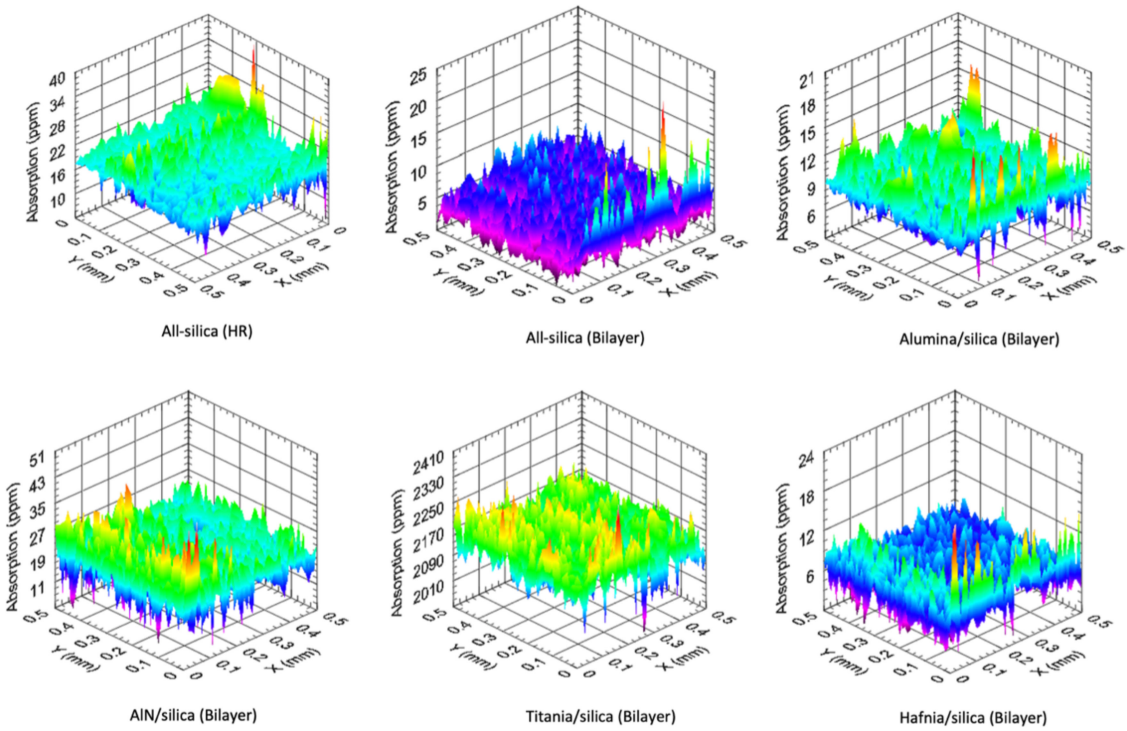

Fig. 6. Surface absorption scans of all-silica multilayered coatings and comparison samples. Absorptions of most samples are low and comparable, except titania/silica sample, which may be deposited oxygen poor.

not follow the expected bandgap dependence was AlN, which showed a much lower LIDT than expected. This was due at least in part to an extreme deviation from expected stoichiometry. An XPS analysis of the sample showed that it contained far more oxygen than nitrogen for reasons which we are still unclear. For this reason, the data points for the pseudo-AlN are not included on the plot. It was noted that all-silica samples showed very little damage or discoloration even at or above 100 kW/cm^2. Heavier damage was noticed only at 500 kW/cm^2, where other materials had long since failed catastrophically.

After the bilayers were tested, multilayer HR samples were tested. As stated previously, all-silica HR samples were fabricated on both thin and thick substrates. Comparison PECVD HR samples were deposited on thin substrates and comparison IBS HR mirrors were fabricated on thick substrates. The majority of laser damage testing on these samples was performed with a 1mm spot size, which provides a large illuminated area, averaging over many contaminants. This spot size allowed peak irradiances up to 3 MW/cm^2. The PECVD samples were designed to have the same difference in refractive indices and same peak wavelength as the all-silica samples. As shown in Fig. 7(b), the all-silica HRs showed contamination-induced damage thresholds at irradiance of 75 kW/cm^2, significantly higher than the PECVD HRs at 25 kW/cm^2.

The thick substrate samples were also tested. All-silica HRs were put down on the same thick fused silica substrates as tantala/silica and hafnia/silica reflectors. HR samples on thick substrates generally have higher LIDT since it is harder for samples to heat rapidly due to the (faster) more three-dimensional heat transfer and higher heat capacity of the thick substrate.

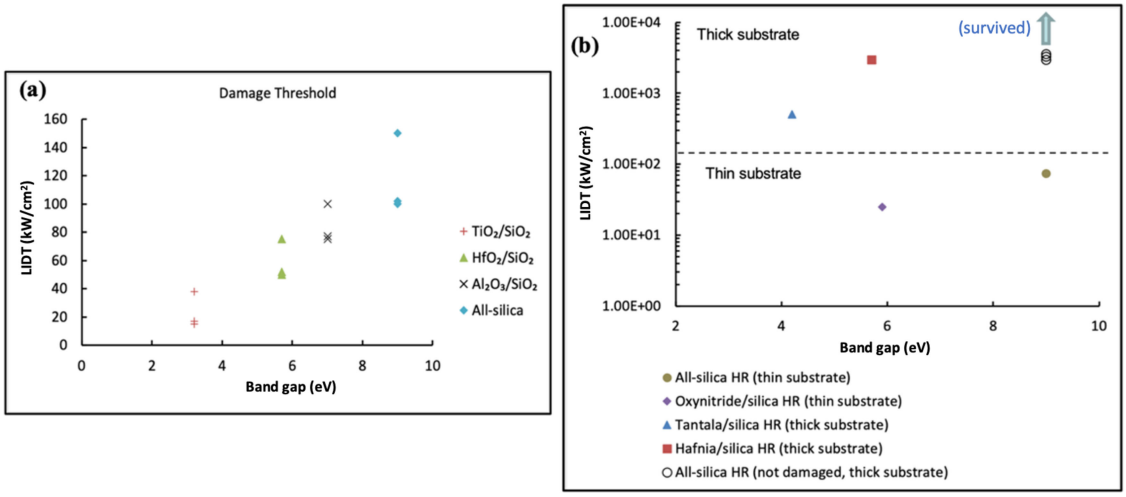

Fig. 7. Contamination-induced LIDT of all-silica multilayer coatings and comparison material coatings. (a) Bilayer samples. The points represent the irradiance at which bilayer samples failed. High data points for each of the sample types are from the first run, in which one sample from each type was tested at varying irradiance levels to estimate their damage thresholds, and low data points are from the second run, in which the rest of the samples were tested at much narrower range of irradiance levels around the initial values, which explains the consistent spread in data. (b) HR coatings on thin and thick substrates. The points represent the irradiance at which HR samples failed, except for the all-silica HR on the thick substrate that survived the highest possible irradiance, represented by an arrow. The all-silica samples showed higher contamination-induced damage thresholds than the other tested materials.

As shown in Fig. 7(b), the all-silica samples had higher LIDTs than the other tested materials. The all-silica samples were shot at three different spots with the highest possible irradiance of 3 MW/cm^2. All three spots survived the shots, with one spot showing slight discoloration, while the hafnia/silica HR, known for its high optical resistance in high power laser applications, failed catastrophically under the same power and contamination conditions. The spot with discoloration may be due to exposure to airborne contaminants in-between layer depositions, which caused a slight haze in that particular area. These results showed that even if the top layer is silica, the contamination-induced LIDT still depends on the bandgap of the materials underneath. Therefore, a multilayered optic made out of a single high bandgap material, silica, as demonstrated here would be expected to show the highest particle-contaminated LIDT under high power CW laser illumination.

Stresses of the all-silica stacks on fused silica substrates were also measured using the film stress measurement system (FSM-900TC). The comparison samples used were bilayer samples, Al_2O_3/SiO_2, HfO_2/SiO_2 and TiO_2/SiO_2, with ALD deposited oxides as bottom layers and evaporated fully-dense silica as top layers, fabricated under similar lab conditions. A total of ten pairs of all-silica layers were deposited. Stress measurements were taken after each single pair (first two measurements) or two pairs of all-silica layers were deposited, both at room temperature and after thermal cycling. Thermal stress changes due to coefficient of thermal expansion (CTE) mismatch were examined by heating the samples to 250 °C, ramping up at 5 °C/min and letting them cool back down naturally to room temperature no faster than 5 °C/min. Stress measurements were made at every 10 °C interval, and each sample was put through three complete heating and cooling cycles. The data, without hysteresis, from the last two cycles, were averaged and used to compare against stresses of the comparison samples at room temperature and also to observe the thermal stress behaviors of all-silica stacks. Fig. 8(a) shows that at room temperature, the stresses of the Al_2O_3/SiO_2, HfO_2/SiO_2 and TiO_2/SiO_2 samples are at 203 MPa, 553 MPa and 516 MPa, while stress of the all-silica stack is approximately 50 MPa, which is significantly lower than ALD-deposited oxides. As expected, the all-silica coatings also showed substantially less thermal expansion mismatch. Changes in thermal stress between room temperature and 250 °C ranged from 15 to 20 MPa for different numbers of pairs of silica as shown in Fig. 8(b). The chaotic shapes of the stress versus temperature curves in Fig. 8(b) are a clear sign that noise was beginning to exceed the small signals due to the almost zero difference in coefficient of thermal expansion (CTE) among all-silica layers and substrate. Due to their low stress and low thermal mismatch properties, the all-silica multilayers may be resistant to stress-related failures.

IV. Conclusion

Low-density layers in all-silica bilayer and HR multilayer samples were fabricated by oblique angle deposition (OAD). All-silica multilayers provide a higher contamination-induced laser damage threshold than comparison materials due to their extremely wide bandgap, and also offer low stress and small thermal expansion mismatch. Bilayer and multilayer HR samples were contaminated with carbon particles for contamination-induced laser damage testing. The bilayer materials showed a strong bandgap dependence, with the all-silica samples having the highest LIDT. HR multilayer samples were tested using thin (0.5 mm) and thick (6.3 mm) substrates. The all-silica HRs on thin substrates showed contamination-induced damage thresholds of 75 kW/cm^2, which is significantly higher than PECVD comparison samples at 25 kW/cm^2. The all-silica HRs on thick substrates survived the highest available irradiance of

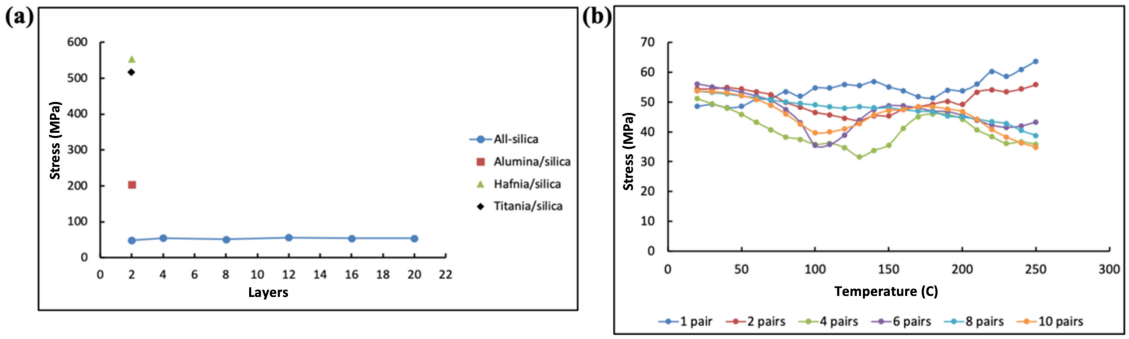

Fig. 8. Stress measurements of an all-silica multilayer (a) at room temperature; stresses of the all-silica sample were significantly lower than ALD-deposited oxide/silica samples, and (b) under annealing conditions; the all-silica multilayer showed low thermal stress changes during cycling from room temperature to 250 °C.

3 MW/cm^2, by which point hafnia/silica HR samples, known for their high optical resistance in high power laser applications, had failed catastrophically. The all-silica multilayers showed low stresses of approximately 50 MPa and low thermal stress changes. Therefore, all-silica coatings offer optical and mechanical advantages that may make them suitable for high power laser applications.

REFERENCES

[1] J. J. W. Hutchinson, "Stresses and failure modes in thin films and multilayers," *Notes Dcamm Course. Tech. Univ. Denmark, Lyngby*, vol. 1, 1996, Art. no. 14.

[2] J. W. Hutchinson and Z. Suo, "Mixed mode cracking in layered materials," *Adv. Appl. Mech.*, vol. 29, pp. 63–191, 1991.

[3] G. Gioia and M. Ortiz, "Delamination of compressed thin films," *Adv. Appl. Mech.*, vol. 33, no. 8, pp. 119–192, 1997.

[4] W. D. Nix, "Mechanical properties of thin films," *Metallurgical Trans. A*, vol. 20, no. 11, 1989, Art. no. 2217.

[5] O. Stenzel, "A model for calculating the effect of nanosized pores on refractive index, thermal shift and mechanical stress in optical coatings," *J. Phys. D: Appl. Phys.*, vol. 42, no. 5, 2009, Art. no. 055312.

[6] M. Laurenti *et al.*, "A porous nanobranched structure: An effective way to improve piezoelectricity in sputtered ZnO thin films," *RSC Adv.*, vol. 6, no. 80, pp. 76996–77004, 2016.

[7] J. L. Hedrick *et al.*, "Templating nanoporosity in thin-film dielectric insulators," *Adv. Mater.*, vol. 10, no. 13, pp. 1049–1053, 1998.

[8] G. San Vicente, R. Bayón, N. Germań, and A. Morales, "Long-term durability of sol–gel porous coatings for solar glass covers," *Thin Solid Films*, vol. 517, no. 10, pp. 3157–3160, 2009.

[9] P. van de Weijer, P. C. Bouten, S. Unnikrishnan, H. B. Akkerman, J. J. Michels, and T. M. van Mol, "High-performance thin-film encapsulation for organic light-emitting diodes," *Org. Electron.*, vol. 44, pp. 94–98, 2017.

[10] K. Chu *et al.*, "Quantitative analysis of nano-defects in thin film encapsulation layer by Cu electrodeposition," *Appl. Surf. Sci.*, vol. 453, pp. 31–36, 2018.

[11] S. S. Kim, N. T. Gabriel, W.-B. Song, and J. J. Talghader, "Encapsulation of low-refractive-index SiO_2 nanorods by Al_2O_3 with atomic layer deposition," *Opt. Exp.*, vol. 15, no. 24, pp. 16285–16291, 2007.

[12] J. Georges, "Continuous-wave-laser versus pulsed-laser excitation for crossed-beam photothermal detection in small volume applications: Comparative features," *Appl. Spectrosc.*, vol. 59, no. 9, pp. 1103–1108, 2005.

[13] J. R. Palmer, "Continuous wave laser damage on optical components," *Opt. Eng.*, vol. 22, no. 4, 1983, Art. no. 224435.

[14] M. F. Doerner and W. D. Nix, "Stresses and deformation processes in thin films on substrates," *Crit. Rev. Solid State Mater. Sci.*, vol. 14, no. 3, pp. 225–268, 1988.

[15] A. Brown, A. Ogloza, L. Taylor, J. Thomas, and J. Talghader, "Continuous-wave laser damage and conditioning of particle contaminated optics," *Appl. Opt.*, vol. 54, no. 16, pp. 5216–5222, 2015.

[16] H. Gong, C. F. Li, and Z. Y. Li, "CW-laser-induced thermal and mechanical damage in optical materials," *Laser-Induced Damage Opt. Mater.: 1998*, vol. 3578, pp. 576–583, 1999.

[17] B. C. Stuart, M. D. Feit, S. Herman, A. M. Rubenchik, B. W. Shore, and M. D. Perry, "Nanosecond-to-femtosecond laser-induced breakdown in dielectrics," *Phys. Rev. B*, vol. 53, no. 4, 1996, Art. no. 1749.

[18] M. Lenzner *et al.*, "Femtosecond optical breakdown in dielectrics," *Phys. Rev. Lett.*, vol. 80, no. 18, 1998, Art. no. 4076.

[19] D. Du, X. Liu, G. Korn, J. Squier, and G. Mourou, "Laser-induced breakdown by impact ionization in SiO_2 with pulse widths from 7 ns to 150 fs," *Appl. Phys. Lett.*, vol. 64, no. 23, pp. 3071–3073, 1994.

[20] J. Jasapara, A. V. V. Nampoothiri, W. Rudolph, D. Ristau, and K. Starke, "Femtosecond laser pulse induced breakdown in dielectric thin films," *Phys. Rev. B*, vol. 63, no. 4, 2001, Art. no. 045117.

[21] A. Brown, D. Bernot, A. Ogloza, K. Olson, J. Thomas, and J. Talghader, "Physical origin of early failure for contaminated optics," *Sci. Rep.*, vol. 9, no. 1, pp. 1–9, 2019.

[22] V. Astašauskas, A. Bellissimo, P. Kuksa, C. Tomastik, H. Kalbe, and W. S. Werner, "Optical and electronic properties of amorphous silicon dioxide by single and double electron spectroscopy," *J. Electron Spectrosc. Related Phenomena*, vol. 241, 2020, Art. no. 146829.

[23] L. Grinevičiūtė *et al.*, "Highly resistant zero-order waveplates based on all-silica multilayer coatings," *Physica Status Solidi*, vol. 214, no. 12, 2017, Art. no. 1700764.

[24] T. Tolenis *et al.*, "Next generation highly resistant mirrors featuring all-silica layers," *Sci. Rep.*, vol. 7, no. 1, pp. 1–9, 2017.

[25] A. Barranco, A. Borras, A. R. Gonzalez-Elipe, and A. Palmero, "Perspectives on oblique angle deposition of thin films: From fundamentals to devices," *Prog. Mater. Sci.*, vol. 76, pp. 59–153, 2016.

[26] D. J. Poxson, F. W. Mont, M. F. Schubert, J. K. Kim, and E. F. Schubert, "Quantification of porosity and deposition rate of nanoporous films grown by oblique-angle deposition," *Appl. Phys. Lett.*, vol. 93, no. 10, 2008, Art. no. 101914.

[27] H. Fujiwara, *Spectroscopic Ellipsometry: Principles and Applications*. Hoboken, NJ, USA: Wiley, 2007.

[28] Y. Toivola, J. Thurn, R. F. Cook, G. Cibuzar, and K. Roberts, "Influence of deposition conditions on mechanical properties of low-pressure chemical vapor deposited low-stress silicon nitride films," *J. Appl. Phys.*, vol. 94, no. 10, pp. 6915–6922, 2003.

[29] W. L. Dang, Y. Q. Fu, J. K. Luo, A. J. Flewitt, and W. I. Milne, "Deposition and characterization of sputtered ZnO films," *Superlattices Microstructures*, vol. 42, no. 1–6, pp. 89–93, 2007.

[30] P. H. Townsend, D. M. Barnett, and T. A. Brunner, "Elastic relationships in layered composite media with approximation for the case of thin films on a thick substrate," *J. Appl. Phys.*, vol. 62, no. 11, pp. 4438–4444, 1987.

[31] M. Ohring, *Materials Science of Thin Films*. Amsterdam, Netherlands: Elsevier, 2001.

[32] E. H. Hirsch, "Stress in porous thin films through absorption of polar molecules (and relevance to optical coatings)," *J. Phys. D: Appl. Phys.*, vol. 13, no. 11, 1980, Art. no. 2081.

[33] Y. Amnon and P. Yeh, *Optical Electronics in Modern Communications*. New York, NY, USA: Oxford Univ. Press, 1997.

[34] A. Alexandrovski, M. Fejer, A. Markosian, and R. Route, "Photothermal common-path interferometry (PCI): New developments," *Solid State Lasers XVIII: Technol. Devices*, vol. 7193, 2009, Art. no. 7193.